J.M. Ribeiro, F.C. Correia, A. Kuzmin, I. Jonane, M. Kong, A.R. Goñi, J.S. Reparaz, A. Kalinko, E. Welter, C.J. Tavares,
Influence of Nb-doping on the local structure and thermoelectric properties of transparent TiO2:Nb thin films,
J. Alloys Compd. 838 (2020) 155561.

Influence of Nb-doping on the local structure and thermoelectric properties of transparent TiO_2:Nb thin films

J.M. Ribeiro[1], F.C. Correia[1], A. Kuzmin[2], I. Jonane[2], M. Kong[5], A. R. Goñi[5,6], J. S. Reparaz[5], A. Kalinko[3,4], E. Welter[4], C.J. Tavares[1]*

[1]Centre of Physics, University of Minho, 4710-057 Braga, Portugal

[2]Institute of Solid State Physics, University of Latvia, LV-1063 Riga, Latvia

[3]Department Chemie, Naturwissenschaftliche Fakultät, Universität Paderborn, Warburger Strasse 100, 33098 Paderborn, Germany

[4]Deutsches Elektronen-Synchrotron − A Research Centre of the Helmholtz Association, Notkestraße 85, D-22607 Hamburg, Germany

[5]Institut de Ciència de Materials de Barcelona-CSIC, Esfera UAB, 08193, Bellaterra, Spain

[6]ICREA, Passeig Lluís Companys 23, 08010 Barcelona, Spain

*Corresponding author: ctavares@fisica.uminho.pt; Telephone: +351 235 510474

Abstract

Transparent n-type niobium-doped titanium dioxide thin films (TiO_2:1.5 at.%Nb) with pronounced thermoelectric properties were produced from a composite Ti:Nb target by reactive magnetron sputtering. The thin films were comprehensively characterized by X-ray diffraction, X-ray photoelectron spectroscopy, optical spectroscopy, electrical conductivity, and thermoelectric measurement techniques. The local structure of the thin films was investigated in detail by X-ray absorption spectroscopy at the Ti and Nb K-edges. A set of radial distribution functions were extracted from the simultaneous analysis of EXAFS data at two absorption edges using the reverse Monte Carlo method. It was found that Nb dopant atoms modify the local environment of the films, but their average structure remains close to that of the anatase phase. This conclusion is also supported by the ab initio simulations of XANES. A very high absolute Seebeck coefficient (S=155 μV/K) for n-type TiO_2 was achieved with Nb doping, yielding a maximum power factor and thermoelectric figure of merit of 0.5 $mW \cdot m^{-1} \cdot K^{-2}$ and 0.18 at a temperature of 300 K, respectively, for a 150 nm thick film. From frequency-domain thermoreflectance experiments, a thermal conductivity value of 1.3 $W \cdot m^{-1} \cdot K^{-1}$ was obtained for the optimized TiO_2:Nb film.

Keywords: Thin films; TiO2:Nb; Seebeck; Thermoelectric; EXAFS; Sputtering

1. Introduction

Transparent conducting oxides (TCOs) are electrically conductive materials with high transparency in the visible range. TCOs have wide-ranging applications in optoelectrical devices including photovoltaics, displays, optoelectrical interfaces and window glass technologies [1]. Touch-screen and solar cell applications require TCO coatings with high transparency (transmissivity >85% when averaged from 400 nm to 1100 nm and weighted by the solar spectrum), combined with useful electrical conductivity (typical resistivity around 10^{-4} Ωcm). In general, to achieve simultaneously the required transmittance and conductivity, the film thickness must be ~150 nm. The most utilized TCO is tin-doped indium oxide (ITO) [2]. Although it is easy to fabricate and possesses good conductive properties, because of its scarcity, poor chemical stability in hydrogen atmosphere and toxicity, there is a huge interest to develop alternative TCOs. Many potential candidates include doped ZnO and SnO_2, amongst other oxide materials, but it is necessary to explore new materials, in particular, thin film-based [3–6].

Recently, thin films have been also widely studied for thermoelectric applications [7]. Thermoelectric materials can convert thermal differences into electrical energy and vice-versa, where the Seebeck coefficient of a material is a measure of the magnitude of an induced thermoelectric voltage in response to a temperature gradient across it. The design of a TCO material with thermoelectric properties is the desired technology for touch–screen displays and solar cell applications, making it possible to produce electrical energy through the harvesting of heat from the environment [8].

Among different materials, titanium dioxide (TiO_2) thin films have interesting structural, optical, electronic and photocatalytic properties, which have been extensively documented in the literature [9]. To further this interest, cationic doping of TiO_2 and $SrTiO_3$ has been documented to improve its electrical conductivity properties [10,11]. In particular, in the present study, Nb-doped TiO_2 thin films were produced and investigated bearing in mind the material potential as a thermoelectric device. Most likely, niobium ions will be present in oxidation states 4+ and 5+ with ionic radii equal to 0.68 Å and 0.64 Å, respectively. It is expected that heavier pentavalent ions added through doping, such as Nb^{5+} in TiO_2, will inhibit the propagation of phonon vibration modes, thus reducing the phononic component of the thermal conductivity below 4 $W{\cdot}m^{-1}{\cdot}K^{-1}$, and increasing the thermoelectric power and figure of merit of the film [12–14]. The choice of Nb for a pentavalent dopant is two-fold. First, the ionic radius of Nb^{5+} (0.64 Å) is slightly higher than that of Ti^{4+} (0.61 Å). Thus, it is suitable to create more phonon scattering and lower the thermal conductivity of the resulting microstructure, without introducing too much stress when the doping is below 5 at.%. Second, when Nb^{5+} substitutes Ti^{4+} in the TiO_2 lattice below the level of solubility, a charge unbalancing occurs, increasing the charge carrier concentration and, thus, also in electrical conductivity [10]. Other pentavalent ions such as vanadium and tantalum have a larger ionic mismatch and are prone to produce other oxides that will compete and inhibit the formation of a stable TiO_2 doped thin film.

2. Experimental details

Nb-doped titanium dioxide thin films with a thickness of 150 nm and 750 nm were deposited in an Ar/O_2 atmosphere at room temperature on Kapton® film (15 mm × 15 mm and 50 μm thick), glass slides (75 mm × 26 mm and 1 mm thick) and silicon substrates (15 mm × 15 mm and 0.5 mm thick) by reactive magnetron sputtering, from a pure Ti:Nb alloy target with 4 wt.% of Nb (FHR, 99.99% purity). Before the depositions, a turbo molecular pump was used to achieve a base pressure of ~10^{-4} Pa. The argon (working gas) and oxygen (reactive gas) flow rates were fixed at 40 sccm and 7.5 sccm, respectively, to attain optimised plasma conditions at a working pressure of 0.35 Pa. During the deposition of these films, the target-to-substrate distance was fixed at 100 mm, the cathode current density was set to 12.7 mA/cm^2, a substrate bias of -60V was applied to the substrate holder, with a temperature of 175 ºC for substrate heating. These deposition conditions enable an effective ~2 at.% of Nb substitutional doping in the TiO_2 cell [10]. Subsequently to deposition, the as-deposited TiO_2:Nb films were annealed in the air for 1 h at 400 ºC.

The thin film samples were comprehensively characterized by X-ray diffraction, X-ray photoelectron spectroscopy, optical spectroscopy, electrical conductivity and thermoelectric measurements.

A Bruker AXS D8 Discover system equipped with the copper anode X-ray tube (CuKα radiation) was used for X-ray diffraction experiments (XRD). The diffraction patterns were collected in the range of 2θ = 22-42° for as-prepared and annealed thin film samples to distinguish between anatase and rutile TiO_2 phases. The X-ray photoelectron spectroscopy measurements were carried out using monochromatic Al-Kα radiation (1486.6 eV) from a Kratos Axis-Supra instrument, from 3Bs Group, University of Minho. Photoelectrons were collected from a take-off angle of 90º relative to the sample surface. The measurement was done in a Constant Analyser Energy mode (CAE) with a 160 eV pass energy and 15 mA of emission current for survey spectra and 40 eV pass energy for high-resolution spectra, using an emission current of 15 mA. Charge referencing was done by setting the lower binding energy of the C1s hydrocarbon peak at 248.8 eV; an electron flood gun was used to minimize surface charging. Spectral transmittance and reflectance responses were measured with a Shimadzu UV-2501PC spectrophotometer, and the band-gap energy was calculated by plotting the squared absorbance versus the photon energy and extrapolating the linear fit of the plot to the photon energy axis [15].

The electrical properties were measured with an Ecopia AMP55T Hall Effect equipment equipped with a four-point probe in van der Pauw method. The Seebeck coefficient was evaluated in custom-made equipment operated in a vacuum (1 Pa) using two Peltier devices (Quick-Ohm Küpper & Co. GmbH) for heating and cooling the edges of 26 mm × 75 mm sample area. The heating and cooling stability was controlled by custom-developed software and hardware. The thermal conductivity of the TiO_2:Nb films was determined using frequency-domain thermoreflectance (FDTR) [16]. This technique is a non-destructive contactless optical method that uses two lasers, pump (405 nm) and probe (532 nm), to locally heat and probe the local temperature, respectively. In order to

enhance the thermal sensitivity of the method, a 60 nm thick Au transducer was evaporated onto the surface of the specimens. Both lasers were focused using an achromatic 30 mm focal distance lens to a spot size of ≈10 μm in diameter. The output power of the pump laser was modulated to a harmonic waveform in the frequency range between 30 kHz and 5 MHz, which generates thermally induced harmonic oscillations of the reflectivity of the sample; thus, leading to a modulation of the reflected power of the continuous wave probe laser. The key quantity that is addressed through this method is the phase lag between the pump heat wave generated by the pump laser, and the harmonic response of the sample as sensed by the probe laser using a lock-in amplifier. The frequency dependent phase lag is modelled numerically solving the parabolic heat equation for the described geometry. The thermal model used to fit the phase lag response curve describes the behaviour of a stack of layers composed by the Au transducer, the studied film, the substrate, and an effective thermal boundary conductance that accounts for the two interfaces defined between the layers. The cross-plane thermal conductivity (κ) and the specific heat capacity (C_p) of the thin films, as well as the substrate-dependant effective thermal boundary conductance of the system were fitted using a least-squares routine. It is important to note that the values of κ and C_p for the Au transducer and the substrates were independently measured, and are used as input parameters in the fitting procedure of the thermal properties of the thin films. In addition, no difference between the in-plane and the out-of-plane components of the thermal conductivity is expected since the typical crystallite size (< 20 nm) is smaller than the thickness of the thin films.

Temperature-dependent X-ray absorption spectroscopy study of TiO_2:Nb thin films was performed to determine the coordination environment of the dopant ions (Nb) and their influence on titanium oxide matrix. Experiments were done in transmission and fluorescence modes at P65 Applied XAFS beamline [17] of the PETRA III storage ring. A set of powder samples (TiO_2, Nb_2O_5) was used for reference. The harmonic rejection was achieved by uncoated and Rh-coated silicon plane mirrors. Fixed exit Si(111) and Si(311) monochromators were used for the Ti and Nb K-edges, respectively. X-ray absorption spectra were collected using two ionization chambers in transmission mode, whereas passivated implanted planar silicon (PIPS) detector was used in fluorescence mode. The Oxford Instruments liquid helium flow cryostat was used to maintain the required sample temperature in the range of 10-300 K. For transmission measurements at the Ti K-edge, a stack of thin films deposited on Kapton was produced, with the number of layers giving the value of the absorption edge jump $\Delta\mu \approx 1$.

3. Data analysis

3.1. Reverse Monte Carlo calculations

X-ray absorption spectra of Nb-doped TiO_2 thin film recorded at the Ti and Nb K-edges were analyzed using the reverse Monte Carlo (RMC) method based on the evolutionary algorithm (EA), implemented in the EvAX code [18]. First, the extended X-ray absorption fine structures (EXAFS) $\chi(k)k^2$ were extracted using a conventional procedure [19]. Strong overlap of the outer coordination shells coupled with the presence of multiple-scattering contributions requires the use of the RMC approach.

Further, simulation boxes (supercells) having different size (4a×4b×2c for pure TiO_2, 5a×5b×2c for TiO_2:Nb) with periodic boundary conditions (PBC) were constructed based on anatase TiO_2 ($I4_1/amd$) crystallographic structure [20]. The size of the box was determined by the concentration of the dopant (Nb) element. RMC/EA calculations were simultaneously performed for 32 atomic configurations. At each iteration, the new atomic configuration was generated by randomly displacing all atoms in the simulation box with the maximally allowed shift of 0.4 Å to get the best possible agreement between the Morlet wavelet transforms (WTs) of the experimental and calculated EXAFS spectra at the Ti and Nb K-edges simultaneously. Note that for pure anatase TiO_2 only data for the Ti-K edge was used. The calculations were performed in the *k*-space range from 2.5 to 13 $Å^{-1}$ and in the *R*-space range from 0.8 to 4.5 Å. No significant improvement in the residual was observed after 5000 iterations. The configuration-averaged EXAFS spectra were calculated by ab initio real-space multiple-scattering (MS) FEFF8.50L code [21,22], including the MS effects up to 4th order. The scattering potential and partial phase shifts were calculated only once within the muffin-tin (MT) approximation [21,22] for the cluster with the radius of 5.5 Å, centred at the absorbing Ti (Nb) atom and constructed based on crystallographic anatase TiO_2 structure [20]. Small variations of the cluster potential due to atom displacements during the RMC/EA simulations were neglected. The photoelectron inelastic losses were accounted for within the one-plasmon approximation using the complex exchange-correlation Hedin-Lundqvist potential [23]. The amplitude reduction factor S_0^2 is included in the scattering amplitude [21,22], calculated by the FEFF code, and no additional correction of the EXAFS amplitude was performed.

3.2. XANES calculations

X-ray absorption near edge structure (XANES) calculations were performed using ab initio real-space FDMNES code [24,25] implementing the finite difference method (FDM). The dipole and quadrupole transitions were taken into account, and the energy-dependent real Hedin-Lundqvist exchange-correlation potential was used [24,25]. The relativistic FDM calculations were performed with self-consistent potential. The calculated XANES spectra were broadened to account for the core-hole level widths (Γ(K-Ti)=0.94 eV and Γ(K-Nb)=4.14 eV) [26] and other multielectronic phenomena. The energy origin was set at the Fermi level E_F. The clusters of different size (radius) were constructed from the crystallographic anatase structure [20] centred at the absorbing Ti atom, which was substituted by Nb to simulated doping.

4. Results and discussion

X-ray diffraction patterns of the as-deposited and thermally annealed TiO_2:Nb thin films deposited on Kapton substrates are shown in Figure 1. A single diffraction peak corresponding to a reflection from the (101) planes of anatase TiO_2 (I41/amd) is discerned at 25.4º, whereas for the thermally annealed film an additional diffraction peak is present at 27.3º, associated with a reflection from the (110) planes of rutile TiO_2 (P42/mnm). The broad background extended to lower diffraction angles is assigned to

the Kapton substrate. The average crystallite size for anatase and rutile phases are 19 and 9 nm, respectively. It should be noted that, experimentally, EXAFS averages over all atoms located both in crystalline and amorphous structures, while XRD amplifies the crystalline domains.

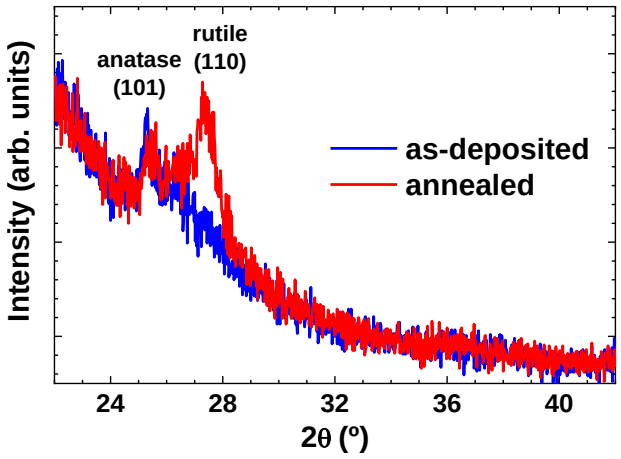

Figure 1. X-ray diffraction patterns of the as-deposited and annealed TiO_2:Nb thin films deposited on Kapton substrates.

To determine the chemical bonding state and film composition, XPS experiments were performed on a TiO_2:Nb thin film, as seen in Figure 2. The main peaks associated with binding energies of 458.9 eV, 530.3 eV and 207.5 eV are ascribed to Ti 2p, O 1s and Nb orbitals [27–29], as listed in Table I.

Peak	Position (eV)	FWHM (eV)	L-S (eV)	L-G	Area ratio	Concentration (at.%)
Ti 2p C1	458.9	1.2	5.7	0.3	2:1	28.7
Ti 2p C1	459.3	1.8	5.7	0.3	2:1	
O 1s C1	530.3	1.3	-	0.2	-	69.8
O 1s C2	532.1	1.3	-	0.2	-	
Nb 3d	207.5	1.1	2.8	0.2	3:2	1.5

Table I. XPS fitting parameters for as-deposited TiO_2:Nb thin film.

The spin-orbital (L-S) splitting is observed for both Ti 2p and Nb 3d core levels, being this splitting 5.7 eV and 2.8 eV, respectively; which is in agreement with the literature. It is also clear that the TiO_2 thin films have been efficiently doped with niobium, since peaks ascribed to binding energies of 207.5 eV are indexed to Nb 3d orbitals, while the L-S doublet separation (16 eV) registered in the survey spectra between 364 eV and 380 eV is attributed to Nb 3p orbitals of pentavalent Nb ions. From this analysis, it was obtained a level of Nb doping of 1.5 at.%. The Ti 2p core-level was fit with two components (C1 and C2) due to the asymmetry of the Ti $2p_{3/2}$ and $2p_{1/2}$ doublet peaks, which is not evident for undoped TiO_2 (not shown). C1 is attributed to Ti-O bonding, as in undoped anatase TiO_2. This asymmetry, registered for the C2 component (6.6% relative contribution), is attributed to the local order around the Ti^{4+} ions, resulting from

Ti-O and Nb-O bonds. As for the O 1s core level, the fit includes two components, C1 and C2, with respective weights of 48.5% and 51.5%, being associated with Ti-O bonds and adsorbed oxygen species at the film surface, respectively. Silicon traces were found in the survey spectra due to the incidence of the beam spot on the sample border, where the Si substrate is exposed. Specific constraints were considered for all XPS fits [28], namely relative area ratio, full width at half maximum (FWHM) and Lorentzian-Gaussian relative profile in doublet peaks.

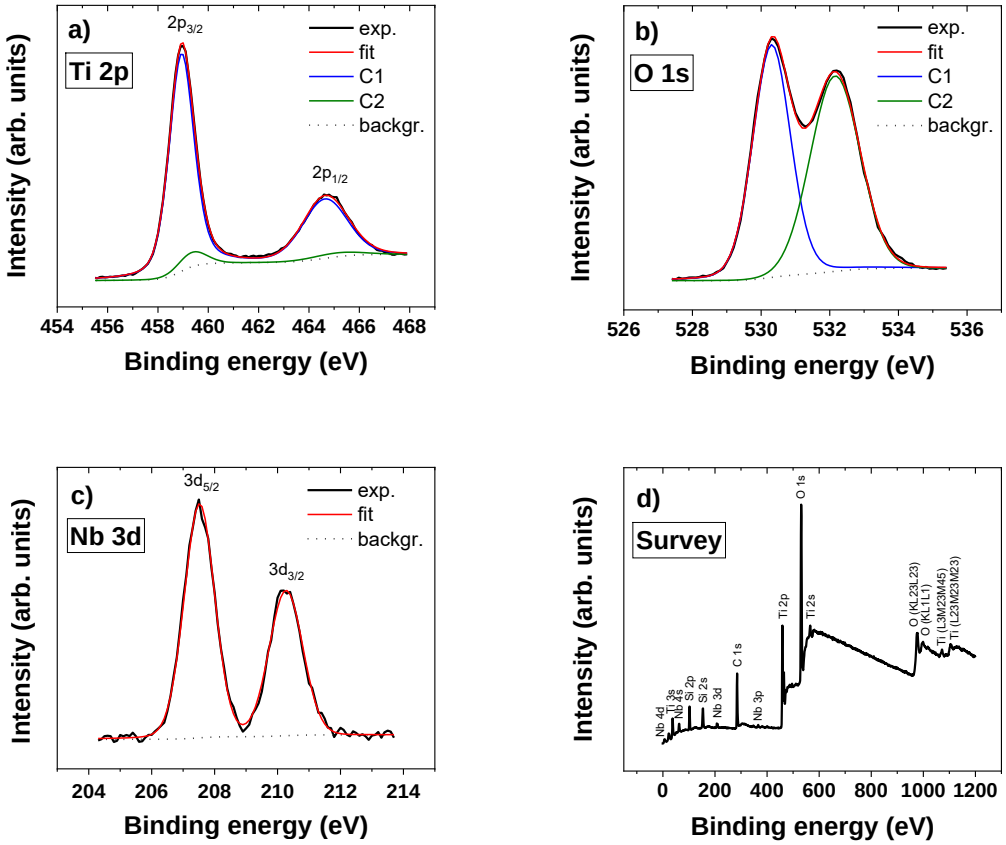

Figure 2. XPS experimental (exp.) spectra and respective fits for a TiO_2:Nb thin film where a) Ti 2p (fitted with 2 components, C1 and C2), b) O 1s (fitted with 2 components, C1 and C2) and c) Nb 3d core levels; in these plots the background (backgr.) is also shown. d) survey spectrum.

The local structure of as-prepared TiO_2:Nb thin film was studied by X-ray absorption spectroscopy. The experimental EXAFS spectra and their Fourier transforms (FTs) at the Ti and Nb K-edges for as-prepared TiO_2:Nb thin film and reference powders (TiO_2 and Nb_2O_5) are shown in Figure 3. A comparison of the EXAFS Ti K-edges in the film and two TiO_2 phases (rutile and anatase) unambiguously indicates the dominant anatase phase in the film. Subsequently, by comparing signals at the Nb K-edge in the film and Nb_2O_5 powder with the signal at the Ti K-edge in anatase TiO_2 powder, one can conclude that the local environment of Nb atoms in the film is close to that of Ti atoms in the anatase phase, but differ significantly from that in Nb_2O_5 powder. This suggests

that the substitution of Ti by Nb ions occurs in the film without a strong influence on the TiO_2 matrix.

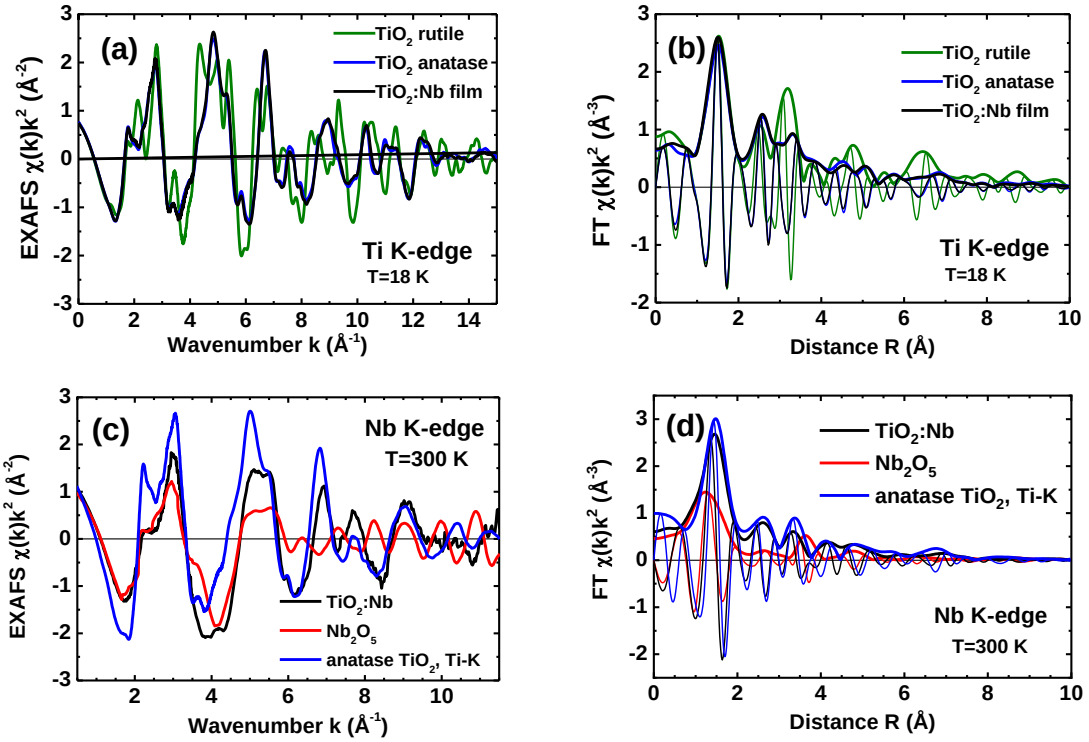

Figure 3. (a) Ti K-edges EXAFS $\chi(k)k^2$ spectra and (b) their Fourier transforms (FTs) at 18 K for rutile and anatase reference powders, and for as-prepared TiO_2:Nb thin film. (c) Ti and Nb K-edges EXAFS $\chi(k)k^2$ spectra and (d) their Fourier transforms (FT) at 300 K for as-prepared TiO_2:Nb thin film (Nb-K edge) and two reference powders – anatase TiO_2 (Ti K-edge) and Nb_2O_5 (Nb K-edge).

Before performing the RMC analysis of EXAFS for the Nb-doped TiO_2 film, an approach was tested using reference anatase TiO_2 powder. Figure 4 shows the experimental and calculated by RMC method Ti K-edge EXAFS spectra $\chi(k)k^2$ and their Fourier and Morlet wavelet transforms for anatase TiO_2 at two different temperatures (18 K and 300 K). The strong interatomic bonding in the anatase phase is responsible for a rather weak temperature dependence of the Ti K-edge EXAFS. However, some EXAFS oscillation damping at high-*k* values occurs upon temperature increase from 18 K to 300 K (Figure 4(a,b)) leading to the peak broadening in FTs (Figure 4(c,d)). The wavelet transforms (WTs) of EXAFS reflect the same thermal disorder effect simultaneously in *k* and *R* space. The WTs are dominated by the first shell contribution of six oxygen atoms (bright spots at R=1.5 Å), whereas titanium atoms of the outer shells are main responsible for the WT complex pattern at longer distances (Figure 4(e,f)).The RMC simulation box was a 4a×4b×2c supercell with anatase TiO_2 structure and PBC, including 128 Ti and 256 O atoms. Hence, the RMC fits reproduce well the temperature-dependence of the Ti K-edge EXAFS spectra and respective WT patterns for anatase TiO_2, so that the EXAFS analysis including the contributions from the coordination shells located as far as up to 4-5 Å can be reliably performed.

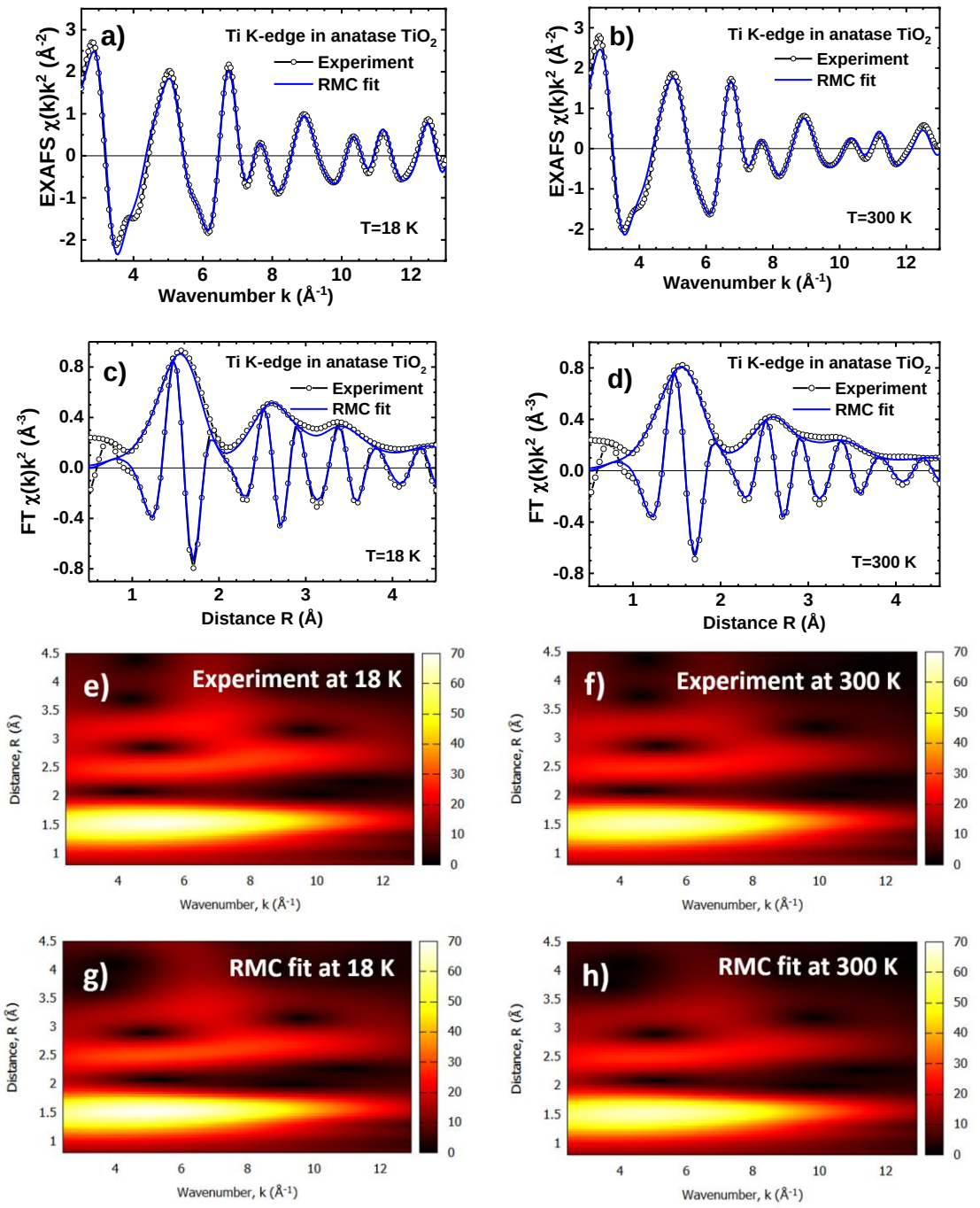

Figure 4. Experimental and calculated by RMC Ti K-edge EXAFS spectra $\chi(k)k^2$ (a, b) and their Fourier (c, d) and Morlet wavelet (e, f, g, h) transforms for anatase TiO_2 reference powder at 18 K and 300 K.

On a subsequent step, the RMC simulations were applied to the simultaneous analysis of the Ti and Nb K-edges EXAFS spectra of TiO_2:Nb thin film at 300 K. The obtained results are shown in Figure 5. The RMC simulation box was a larger 5a×5b×2c supercell with anatase TiO_2 structure comprising 10% of Ti atoms substituted randomly by Nb atoms, resulting in a total of 180 Ti, 20 Nb and 400 O atoms in the supercell. As in the case of anatase TiO_2, the RMC simulation fits very well the experimental data of TiO_2:Nb thin film at both edges simultaneously and over a large (more than 4 Å)

distance range in *R*-space. Note that in this case, the single structural model can describe well the environment around both Ti and Nb atoms taking into account the structure relaxation due to a difference in the Ti-O and Nb-O bonding. The similarity of the local atomic structure around Ti and Nb atoms in the TiO_2:Nb thin film is well reflected by close WT patterns (Figure 5(e,f)), which are well reproduced in the RMC simulations (Figure 5(g,h)). Similar RMC simulations (not shown), with 5% of substituting Nb atoms and including 190 Ti, 10 Nb and 400 O atoms in the supercell, gave close agreement with the experimental data.

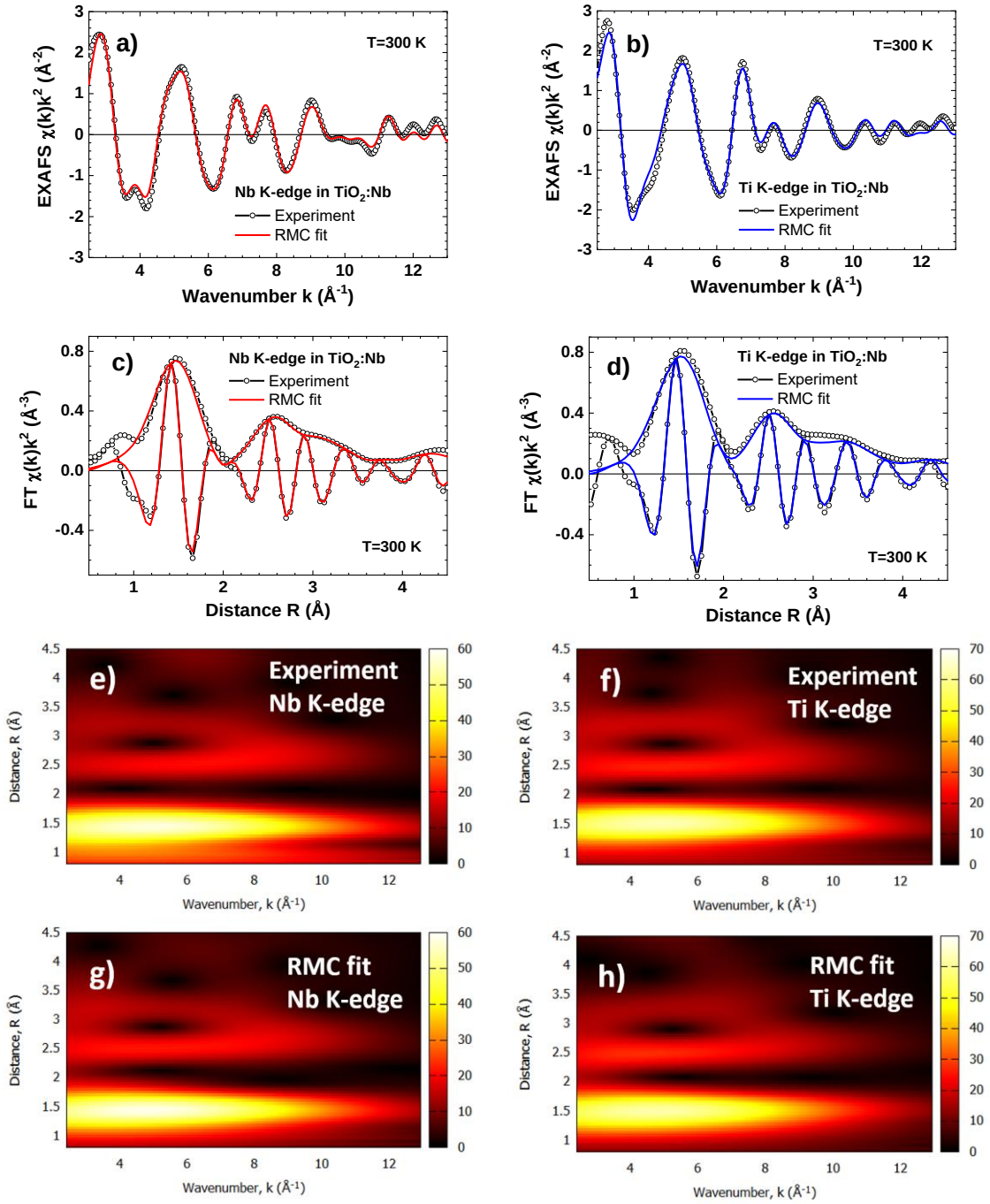

Figure 5. Experimental and calculated by RMC Ti and Nb K-edge EXAFS spectra $\chi(k)k^2$ (a, b) and their Fourier (c, d) and Morlet wavelet (e, f, g, h) transforms for TiO_2:Nb thin film at 300 K.

The atomic coordinates obtained in the RMC simulations of the TiO_2:Nb thin film with 5% and 10% of dopant Nb atoms at 300 K were used to calculate the radial distribution functions (RDFs) *G*(R) for Nb-O, Nb-Ti, Ti-O and Ti-Ti atom pairs. They are shown in Figure 6(a, b) in comparison with the RDFs *G*(Ti-O) and *G*(Ti-Ti) for anatase TiO_2. To improve statistics, the RDFs were evaluated as an average over six independent RMC calculations. The two models with different percentage of Nb doping give close RDFs. Also, the RDFs *G*(Ti-O) and *G*(Ti-Ti) are rather close in the thin film and anatase suggesting that doping by niobium does not change significantly the local environment of Ti atoms.

A comparison of the RDFs *G*(Nb-O) and *G*(Ti-O) in the thin film indicates that both Nb and Ti atoms are octahedrally coordinated by oxygen atoms. However, Nb environment relaxes leading to a larger splitting of the first coordination shell than that in the anatase structure. The first shell of Ti atoms in anatase is split into two groups (3+3) of oxygen atoms located at 1.93 Å and 1.98 Å [20]. In our RMC calculations, the first shell of Ti atoms in both film and anatase does not split and is represented by a broad peak centered at ~1.95 Å. At the same time, the larger distortion of Nb environment leads to its first shell splitting into two groups (3+3) of oxygen atoms at ~1.88 Å and ~2.01 Å. Note that the second coordination shell of Nb (peak at 3 Å in Figure 6(a,b)) is also displaced slightly compared to that of Ti but to longer distances. The average values of the Nb-Ti and Ti-Ti distances are 3.11 Å and 3.04 Å, respectively. Thus, doping by Nb atoms modifies the local environment in the film; however, its average structure still resembles that of anatase (Figure 6(c, d)).

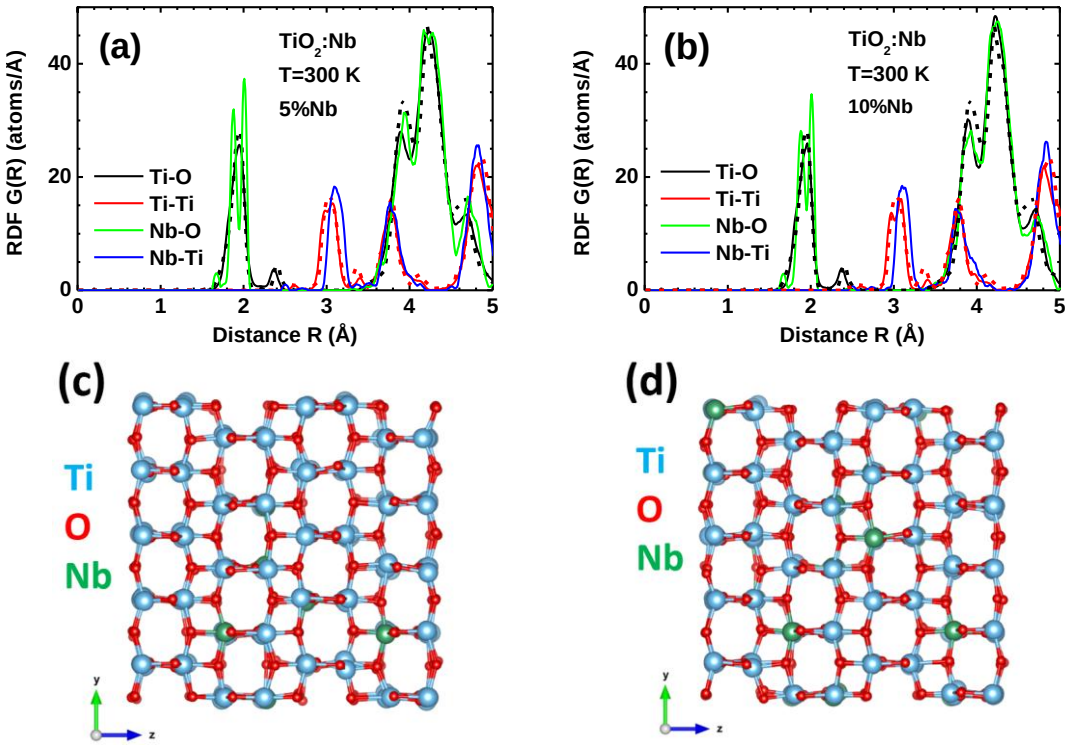

Figure 6. (a, b) Radial distribution functions (RDFs) G(R) calculated from the coordinates of atoms in a TiO_2 5×5×2 supercell at 300K, for 5% and 10% of dopant Nb atoms. Dashed (black and red) curves are for RDFs *G*(Ti-O) and *G*(Ti-Ti) in anatase TiO_2 at T=300 K. (c, d) Fragments of the RMC 5a×5b×2c supercells for c) 5% of Nb and d) 10% of Nb atoms.

The X-ray absorption near edge structure (XANES) spectra of TiO_2:Nb thin film measured at the Ti and Nb K-edges are presented in Figure 7. XANES spectra are better resolved at the Ti K-edge due to the smaller value of the core-level width (Γ(K-Ti)=0.94 eV vs Γ(K-Nb)=4.14 eV) [26]. This makes a difference mainly in the pre-edge region at 0-10 eV above the Fermi level. The main variance around 20 eV comes from the difference in the Ti(Nb) p-orbitals density of states (p-DOS, as seen later on). Note also that there is a slight difference in the fine structure above the two edges due to some modification of the local environment around Ti and Nb atoms caused by a difference in the Ti-O and Nb-O bonding. The Ti K-edge XANES spectra of the thin film and reference anatase TiO_2 powder are very similar, suggesting resemblances of their local environment in agreement with the results of our EXAFS analysis.

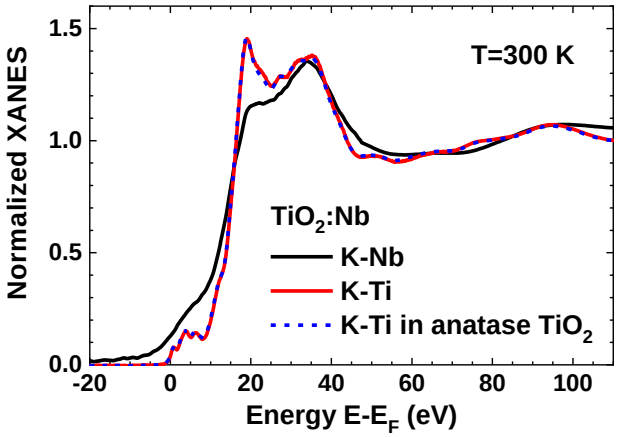

Figure 7. Experimental XANES spectra of TiO_2:Nb thin film at the Ti and Nb K-edges measured at 300K. The Ti K-edge XANES spectrum (dashed line) of reference anatase TiO_2 powder is shown for comparison.

To understand the origin of the XANES features, theoretical simulation using ab initio FDMNES code [24,25] were performed using the finite difference method. This approach, while being more computationally time-consuming, gives better results in the case of the distorted environment, as in the case of both pure and Nb-doped TiO_2, than the Green function formalism with spherical muffin-tin potentials. Note also that the origin of XANES features above the absorption edge is due to the dipole-allowed transitions from 1s(Ti/Nb) core state to unoccupied p-states, whereas three pre-edge peaks have mixed quadrupole-dipolar origin, involving d-metal states in the conduction band [30].

Experimental XANES spectra of TiO_2:Nb thin film at 300 K measured at the Ti and Nb K-edges are compared with those calculated by ab initio FDMNES code in Figure 8. A good agreement is observed for both Ti and Nb K-edges XANES for the cluster radius of 8.1 Å. However, main XANES features are reproduced already for the small cluster (4.0 Å) containing four coordination shells. It is interesting to note that, despite of similarities of the local structure around Nb and Ti atoms, their XANES spectra differ appreciably in the range of 15-40 eV above the edge, where the two main peaks have opposite amplitude. At the Ti K-edge, the peak at ~20 eV is more intense than the peak

at ~35 eV, whereas, at the Nb K-edge, the situation is the opposite, i.e. the peak at ~20 eV has a smaller amplitude than that at ~35 eV. To understand the origin of this difference, a more detailed analysis was performed. First, it was studied the influence of the core-level width on the shape of XANES. The results of the Nb K-edge XANES simulations with the two core-level widths Γ=0.94 eV and 4.14 eV [26] corresponding to the Ti and Nb K-edges, respectively, are shown in Figure 9(a). The small pre-edge peak located just above the Fermi level is related to mixed Ti d-states and O p-states in the conduction band. As one can see, the reduction of the natural broadening influences the sharpness of all features but does not change their relative amplitudes. At the same time, the observed differences in the XANES at two absorption edges correlate well with the partial unoccupied DOS probed by 1s electron, i.e. p(Ti/Nb)-DOS, shown in Figure 9(b). Also, in Figure 9(b) the opposite amplitude effect that is registered for the two main peaks at the Ti and Nb K-edges is more evident (highlighted by the blue oval shapes).

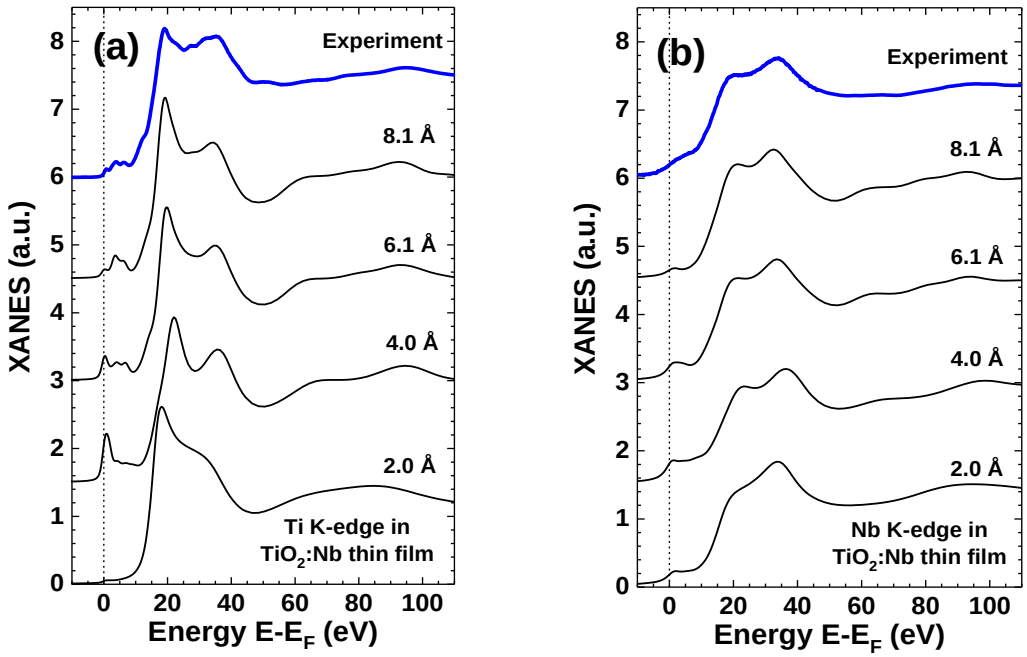

Figure 8. Experimental and calculated XANES spectra of TiO_2:Nb thin film measured at the Ti (a) and Nb (b) K-edges at 300K. The calculations were performed for varying atomic cluster sizes. The spectra are vertically shifted for clarity.

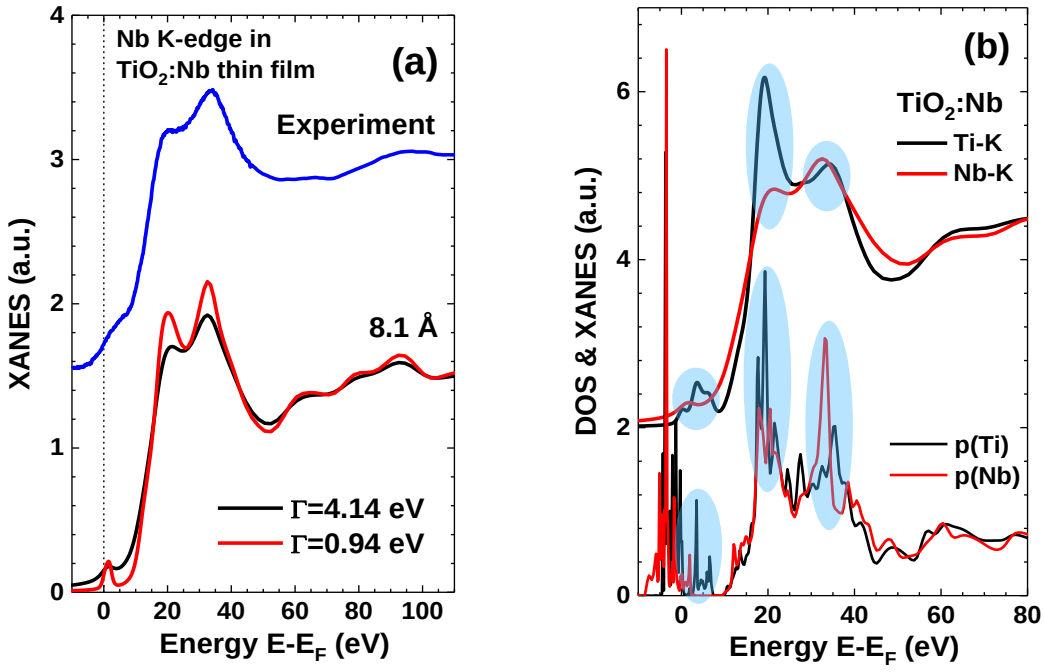

Figure 9. (a) Experimental and calculated Nb K-edge XANES spectra of TiO_2:Nb thin film. The calculations were performed for the cluster radius of 8.1 Å and two different core-level widths Γ=0.94 eV and 4.14 eV. (b) A comparison of the calculated XANES spectra at the Ti and Nb K-edges (top) with p-DOS for Ti and Nb (bottom).

The measured thermal, thermoelectric, electrical and optical properties of the TiO_2:Nb film deposited on glass and Si substrates are presented in Table II, and were experimentally determined as described in Section 2. A very high absolute Seebeck coefficient, S=155 μV/K, for n-type TiO_2 was achieved with Nb doping for the thinner film (150 nm). For the thicker film (750 nm), a 65% lower value, S=101 μV/K, was obtained. These Seebeck coefficients were determined from, the slope of the ΔV vs. ΔT and the respective experimental errors are listed in Table II. In Figure 10, the Seebeck coefficient values were measured for both of these films at 5 K step values with a stabilization of 60 min. per step, integration time of 40 min. at that step, in order to thermally stabilize both ends of the sample. These S step values are a bit lower for the thicker film when compared to that obtained for the whole temperature gradient range (from the aforementioned slopes) due to a small potential offset originated at the start of the experiment. This variation in S for both films is further elucidated later in the manuscript when discussing the electrical properties. It is noteworthy to mention that this magnitude of the Seebeck effect was registered within a relatively small thermal gradient of 50 K across the film surface (75 mm × 26 mm), for a 750 nm thick film. This thermal gradient is more than the authors expect for applications of these films as thermal energy harvesters in touch displays or photovoltaic cells. The resulting power factor (PF) and figure of merit (ZT) were calculated using the following expressions $S^2\sigma$ and $S^2\sigma T/\kappa$, respectively, where σ is the electrical conductivity, T is temperature and κ is the thermal conductivity of the TiO_2:Nb film. PF and ZT values at 300K of 0.5 $mW \cdot m^{-1} \cdot K^{-2}$ and 0.18, respectively, were obtained for optimized (150 nm) TiO_2:Nb films; which for transparent thin films excels what is commonly found in the literature.

The data in Table II were recorded from a large collection of similar samples; hence, the registered uncertainty in some properties, such as thermal and electrical conductivities. The value of the thermal conductivity measured by FDTR at 300 K is 1.3 $W \cdot m^{-1} \cdot K^{-1}$ and 2.3 $W \cdot m^{-1} \cdot K^{-1}$, for 150 nm and 750 nm thick TiO_2:Nb films, respectively. The values of κ are quite low compared to what is known for undoped TiO_2 (5-10 $W \cdot m^{-1} \cdot K^{-1}$) [31]. From the fit of the phase lag data in Figure 11, for both a) 150 nm and b) 750 nm TiO_2:Nb thick films, it was possible to calculate κ, with a maximum uncertainty of ± 0.3 $W \cdot m^{-1} \cdot K^{-1}$. Also, from these fits, values for C_p of 1200 $J \cdot kg^{-1} \cdot K^{-1}$ and 1050 $J \cdot kg^{-1} \cdot K^{-1}$were obtained for 150 nm and 750 nm thick TiO_2:Nb films, respectively, which is in agreement with the variation in κ.

As comparison with the present results, Min-Hee Hong [32]and co-workers published ZT Values lower than 0.01 for mesoporous TiO_2 sol-gel films, without disclosing thickness. In a similar deposition process, Ling Xu and co-workers [33] prepared 320 nm thick TiO_2:Al films, with Al varying from 0 - 5 at.%, also presenting ZT values lower than 0.01. Kurita et al. [34] reported thermoelectric power factors in the range of 0.25 $mW \cdot m^{-1} \cdot K^{-2}$ at 900K for heavily Nb-doped TiO_2 epitaxial films deposited at 800K by pulse-laser deposition (PLD) with similar thickness, about 50% of the value obtained in this work, albeit with similar S values, 145 μV/K. Moreover, the latter PF value was assessed at the triple of the temperature measured for the present TiO_2:Nb thin films, which are polycrystalline and were deposited below 450K, in order to meet industrial applications. On the other hand, Ohta et al. [35] obtained a much higher PF and ZT values at 1000 K, ~1.5 $mW \cdot m^{-1} \cdot K^{-2}$ and ~0.3, respectively, for ~100 nm thick $SrTiO_3$ films deposited by PLD at ~1000K, nonetheless with a much higher Nb content (40 at.%). No information in transmittance levels of the films is given for both literature references.

The average values at 300 K for electrical conductivity, n-type carrier concentration and mobility for TiO_2:Nb films are also displayed in Table II. The thicker film has a higher electrical conductivity, 992 $(\Omega \cdot cm)^{-1}$, when compared to the thinner one, 219 $(\Omega \cdot cm)^{-1}$, as it would be expected. This explains why the Seebeck coefficient and thermal conductivity is higher in the thinner film, as mentioned in the last paragraph, since the number of impurities and defects (Nb^{5+} dopant ions, ionized oxygen vacancies) is lower, owing to the lower carrier concentration (~10^{20} cm^{-3}) and higher mobility (26 $cm^2 \cdot V^{-1} \cdot s^{-1}$), when compared to the thicker film, in Table II. Moreover, for the thinner film, electron and phonon scattering is increased, due to decrease both in σ and κ, hence resulting a a larger separation of charges between the hot and cold sides, and thus the increase in S. For the thicker film, the net result of cationic pentavalent doping of Nb in TiO_2 results in a substantial enhancement of transport properties due to charge unbalancing and oxygen vacancies creation [36], which concomitantly impacts on the increase in PF. Also, with the increase in impurities in TiO_2 for the thicker film, the mobility is reduced [37].

Table II. Thermoelectric, thermal, electrical and optical properties of TiO_2:Nb film for different thickness: Seebeck coefficient (S); thermoelectric power factor (PF) and figure of merit (ZT); thermal conductivity (κ); electrical conductivity (σ), carrier concentration (n) and mobility (μ); optical band-gap (E_g).

Thick (nm)	S ($\mu V \cdot K^{-1}$)	PF ($mW \cdot m^{-1} \cdot K^{-2}$)	ZT	κ ($W \cdot m^{-1} \cdot K^{-1}$)	σ $(\Omega \cdot cm)^{-1}$	n (cm^{-3})	μ ($cm^2 \cdot V^{-1} \cdot s^{-1}$)	E_g (eV)
150	-155±2	0.5±0.1	0.18±0.05	1.3±0.2	$(2.19\pm0.02)\times10^2$	$(8\pm2)\times10^{19}$	26±10	3.27±0.01
750	-101±2	1.0±0.1	0.13±0.02	2.3±0.3	$(9.92\pm0.01)\times10^2$	$(4\pm2)\times10^{21}$	2±1	3.24±0.01

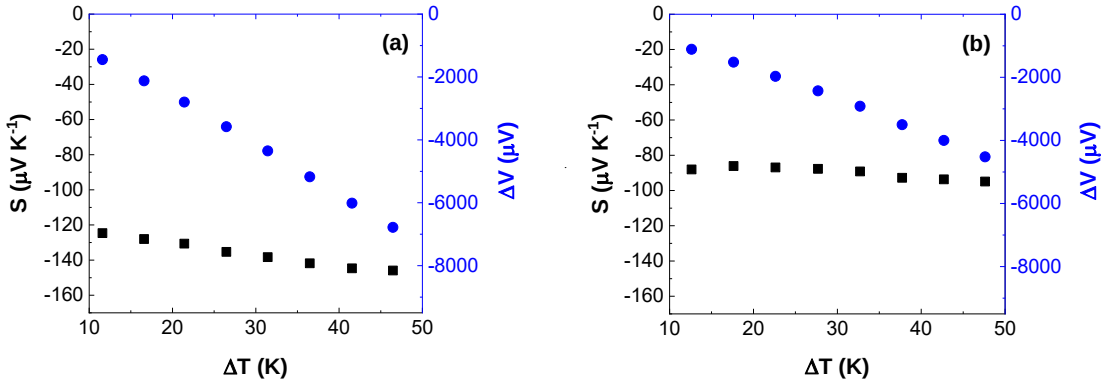

Figure 10. Evolution of the Seebeck coefficient (squares) and potential difference (dots) with a thermal gradient across the surface of a 75 mm × 26 mm, for a) 150 nm and b) 750 nm thick, TiO_2:Nb film on a glass substrate.

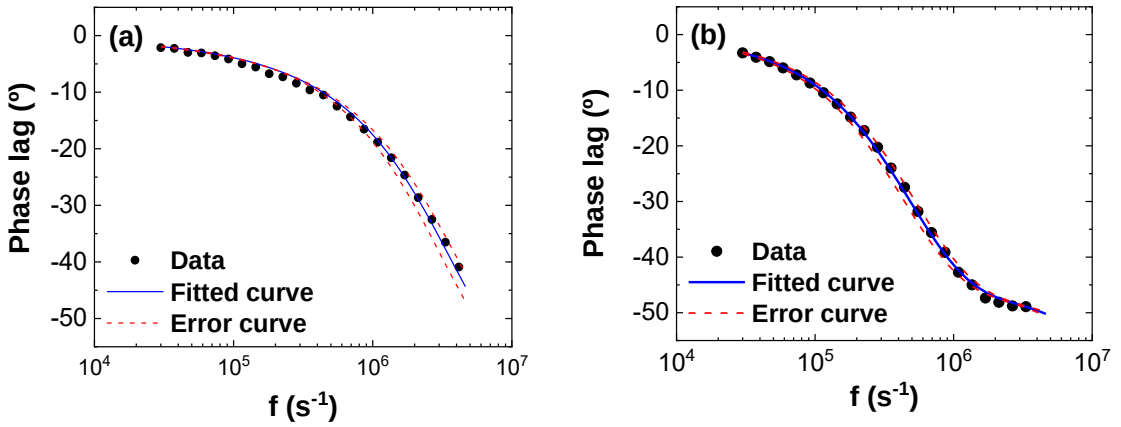

Figure 11. Frequency-dependent phase lag between the pump (405 nm) and probe (532 nm) lasers for a) 150 nm and b) 750 nm thick TiO_2:Nb thin film. The results from the fits are listed in Table II. Error curves represents ±0.2 and ±0.3 uncertainty in κ for a) and b), respectively.

The TiO_2:Nb semiconductor band-gap (E_g) was derived from the measurement of optical transmittance and reflectance and subsequent calculation of the absorption

coefficient (α), as presented in the Tauc plot in Figure 12. From the intercept of the linear decay of α with the photon energy axis, a value of E_g=3.24 eV was determined a 750 nm thick TiO_2:Nb film, which is slightly higher than that known for undoped TiO_2 (3.20 eV) [38]. The slight increase in E_g is attributed to the Burstein-Moss effect [39] and can be explained through the Pauli Exclusion Principle, where a broadening of the band-gap is observed with increasing doping. This shift arises because the Fermi energy lies in the conduction band for heavy n-type doping (as is the case for TiO_2:Nb). The filled states, therefore, block thermal or optical excitation. Consequently, the measured band gap determined from the onset of interband absorption moves to higher energy (i.e. blue shift).

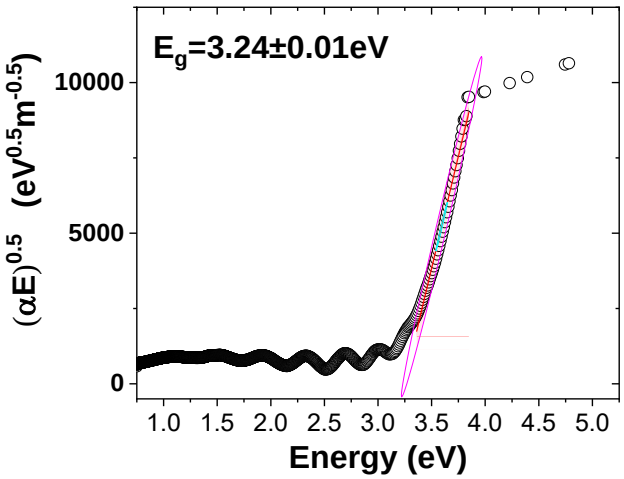

Figure 12. Determination of the optical band-gap of the TiO_2:Nb thin film deposited on glass, 750 nm thick. The ellipse shows a region within 95% confidence for the linear regression.

5. Conclusions

Transparent n-type niobium-doped titanium dioxide thin films (TiO_2:Nb), with an optical band-gap of 3.21-3.24 eV, were successfully produced by reactive magnetron sputtering from a composite Ti:Nb target in an oxygen atmosphere. An amount of 1.5 at.%. Nb doping was estimated from X-ray photoelectron spectroscopy experiments. Optimized Nb-doped films exhibit pronounced thermoelectric properties with a very high absolute Seebeck coefficient of 155 μV/K for a 150 nm thickness. The maximum power factor (PF) and figure of merit (ZT) values of 0.5 $mW \cdot m^{-1} \cdot K^{-2}$ and 0.18, respectively, were obtained for TiO_2:Nb films with a thermal conductivity of 1.3 $W \cdot m^{-1} \cdot K^{-1}$, which excels what is commonly found in the literature for transparent thin films.

Structural investigations by X-ray diffraction and X-ray absorption spectroscopy at the Ti and Nb K-edges were performed to elucidate the role of Nb dopant on the film structure and properties. The as-deposited films possess anatase TiO_2 phase evidenced by XRD, however, the rutile phase is additionally formed upon film thermal annealing at 400 °C. Detailed information on the local structure of the thin films was obtained in terms of the radial distribution functions determined from the simultaneous analysis of

EXAFS data at two absorption edges using the reverse Monte Carlo method. It was concluded that the local environment of the thin films is affected by Nb doping, however, their average local structure remains close to that of the anatase TiO_2 phase. This result is also supported by the analysis of XANES using ab initio simulations.

Acknowledgements

The experiment at HASYLAB/DESY was performed within the project I-20180036 EC. The research leading to this result has been supported by the project CALIPSOplus under the Grant Agreement 730872 from the EU Framework Programme for Research and Innovation HORIZON 2020. Filipe Correia is grateful to the *Fundação para a Ciência e Tecnologia* (FCT, Portugal) for the Ph.D. Grant SFRH/BD/111720/2015. Joana Ribeiro is grateful to the Project WinPSC - POCI-01-0247-FEDER-017796, for the research grant, co-funded by the European Regional Development Fund (ERDF), through the Operational Programme for Competitiveness and Internationalisation (COMPETE 2020), under the PORTUGAL 2020 Partnership Agreement. The authors acknowledge the funding from the following institution Fundação para a Ciência e Tecnologia (FCT, Portugal) / PIDDAC through the Strategic Funds project reference UID/FIS/04650/2013. The Spanish Ministry of Economy, Industry, and Competitiveness through the "Severo Ochoa" Program for Centers of Excellence in R&D (SEV-2015-0496), projects No. MAT2017-90024-P (TANGENTS)-EI/FEDER and MAT2015-70850-P (HIBRI2), and the Generalitat de Catalunya through grant 2017-SGR-00488. M. K. acknowledges the Ph.D. programme in Materials Science from Universitat Autonoma de Barcelona in which she is enrolled.

References

[1] C.I. Bright, Review of Transparent Conductive Oxides (TCO) , 3M Company, Tuscon, Arizona, in: 50 Years Vac. Coat. Technol. Growth Soc. Vac. Coaters, Springer, Cham, 2007. doi:https://doi.org/10.1007/978-3-319-48933-9_58.

[2] T. Minami, Transparent conducting oxide semiconductors for transparent electrodes, Semicond. Sci. Technol. 20 (2005) S35--S44. doi:10.1088/0268-1242/20/4/004.

[3] S.-M. Park, T. Ikegami, K. Ebihara, P.-K. Shin, Structure and properties of transparent conductive doped ZnO films by pulsed laser deposition, Appl. Surf. Sci. 253 (2006) 1522–1527. doi:10.1016/j.apsusc.2006.02.046.

[4] Ü. Özgür, Y.I. Alivov, C. Liu, A. Teke, M.A. Reshchikov, S. Doğan, V. Avrutin, S.J. Cho, H. Morkoç, A comprehensive review of ZnO materials and devices, J. Appl. Phys. 98 (2005) 1–103. doi:10.1063/1.1992666.

[5] M.W. Gaultois, T.D. Sparks, C.K.H. Borg, R. Seshadri, W.D. Bonificio, D.R. Clarke, Data-driven review of thermoelectric materials: Performance and resource onsiderations, Chem. Mater. 25 (2013) 2911–2920. doi:10.1021/cm400893e.

[6] K. Koumoto, I. Terasaki, R. Funahashi, Complex Oxide Materials for Potential Thermoelectric Applications, MRS Bull. 31 (2011) 206–210. doi:10.1557/mrs2006.46.

[7] T.M. Tritt, M. a. Subramanian, Thermoelectric Materials, Phenomena, and

Applications: A Bird's Eye View, MRS Bull. 31 (2006) 188–198. doi:10.1557/mrs2006.44.

[8] G.A. Slack, New Materials and Performance Limits for Thermoelectric Cooling, in: D.M. Rowe (Ed.), CRC Handb. Thermoelectr., 1st ed., CRC Press, 1995. doi:doi:10.1201/9781420049718.ch34.

[9] A. Fujishima, X. Zhang, D.A. Tryk, Surface Science Reports TiO 2 photocatalysis and related surface phenomena, 63 (2008) 515–582. doi:10.1016/j.surfrep.2008.10.001.

[10] M. V. Castro, L. Rebouta, P. Alpuim, M.F. Cerqueira, M. Benelmekki, C.B. Garcia, E. Alves, N.P. Barradas, E. Xuriguera, C.J. Tavares, Optimisation of surface treatments of TiO 2 : Nb transparent conductive coatings by a post-hot-wire annealing in a reducing H 2 atmosphere, Thin Solid Films. 550 (2014) 404–412. doi:10.1016/j.tsf.2013.11.044.

[11] S. Ohta, T. Nomura, H. Ohta, M. Hirano, H. Hosono, K. Koumoto, Large thermoelectric performance of heavily Nb-doped SrTiO3 epitaxial film at high temperature, Appl. Phys. Lett. 87 (2005) 092108/1-092108/3. doi:10.1063/1.2035889.

[12] F.C. Correia, P.B. Salvador, J.M. Ribeiro, A. Mendes, C.J. Tavares, Effect on the electrical and morphological properties of Bi incorporation into ZnO:Ga and ZnO:Al thin films deposited by confocal magnetron sputtering, Vacuum. 152 (2018) 252–260. doi:10.1016/j.vacuum.2018.03.033.

[13] F.A. Zhao, H.Y. Xiao, X.M. Bai, Z.J. Liu, X.T. Zu, Effects of doping Yb3+, La3+, Ti4+, Hf4+, Ce4+ cations on the mechanical properties, thermal conductivity, and electronic structures of Gd2Zr2O7, J. Alloys Compd. 776 (2019) 306–318. doi:10.1016/J.JALLCOM.2018.10.240.

[14] S. Bhattacharya, A.M. Dehkordi, H.N. Alshareef, T.M. Tritt, Synthesis–property relationship in thermoelectric $Sr_{1-x}Yb_xTiO_{3-\delta}$ ceramics, J. Phys. D. Appl. Phys. 47 (2014) 385302. doi:10.1088/0022-3727/47/38/385302.

[15] J. Tauc, R. Grigorovici, A. Vancu, Optical Properties and Electronic Structure of Amorphous Germanium, Phys. Status Solidi. 15 (1966) 627–637. doi:10.1002/pssb.19660150224.

[16] A.J. Schmidt, R. Cheaito, M. Chiesa, A frequency-domain thermoreflectance method for the characterization of thermal properties, Rev. Sci. Instrum. 80 (2009). doi:10.1063/1.3212673.

[17] E. Welter, R. Chernikov, M. Herrmann, R. Nemausat, A beamline for bulk sample x-ray absorption spectroscopy at the high brilliance storage ring PETRA III, AIP Conf. Proc. 2054 (2019) 1–6. doi:10.1063/1.5084603.

[18] J. Timoshenko, A. Kuzmin, J. Purans, EXAFS study of hydrogen intercalation into ReO3 using the evolutionary algorithm, J. Phys. Condens. Matter. 26 (2014). doi:10.1088/0953-8984/26/5/055401.

[19] A. Kuzmin, J. Chaboy, EXAFS and XANES analysis of oxides at the nanoscale, IUCrJ. 1 (2014) 571–589. doi:10.1107/S2052252514021101.

[20] C.J. Howard, T.M. Sabine, F. Dickson, Structural and thermal parameters for

rutile and anatase, Acta Crystallogr. Sect. B Struct. Sci. 47 (1991) 462–468. doi:10.1107/S010876819100335X.

[21] A.L. Ankudinov, B. Ravel, J.J. Rehr, S.D. Conradson, Real-space multiple-scattering calculation and interpretation of x-ray-absorption near-edge structure, Phys. Rev. B. 58 (1998) 7565–7576. doi:10.1103/PhysRevB.58.7565.

[22] J.J. Rehr, R.C. Albers, Theoretical approaches to x-ray absorption fine structure, Rev. Mod. Phys. 72 (2000) 621–654. doi:10.1103/RevModPhys.72.621.

[23] L. Hedin, B.I. Lundqvist, Explicit local exchange-correlation potentials, J. Phys. C Solid State Phys. 4 (1971) 2064–2083. doi:10.1088/0022-3719/4/14/022.

[24] Y. Joly, X-ray absorption near-edge structure calculations beyond the muffin-tin approximation, 63 (2001) 1–10. doi:10.1103/PhysRevB.63.125120.

[25] O. Bunau, Y. Joly, Self-consistent aspects of x-ray absorption, (2009). doi:10.1088/0953-8984/21/34/345501.

[26] O. Keski-Rahkonen, M.O. Krause, Total and partial atomic-level widths, At. Data Nucl. Data Tables. 14 (1974) 139–146. doi:10.1016/S0092-640X(74)80020-3.

[27] M.Z. Atashbar, H.T. Sun, B. Gong, W. Wlodarski, R. Lamb, XPS study of Nb-doped oxygen sensing TiO2 thin films prepared by sol-gel method, Thin Solid Films. 326 (1998) 238–244. doi:10.1016/S0040-6090(98)00534-3.

[28] M.C. Biesinger, L.W.M. Lau, A.R. Gerson, R.S.C. Smart, Resolving surface chemical states in XPS analysis of first row transition metals, oxides and hydroxides: Sc, Ti, V, Cu and Zn, Appl. Surf. Sci. 257 (2010) 887–898. doi:10.1016/j.apsusc.2010.07.086.

[29] A. Mattsson, M. Leideborg, K. Larsson, G. Westin, L. Österlund, Adsorption and Solar Light Decomposition of Acetone on Anatase TiO_2 and Niobium Doped TiO_2 Thin Films, J. Phys. Chem. B. 110 (2006) 1210–1220. doi:10.1021/jp055656z.

[30] Y. Joly, D. Cabaret, H. Renevier, C.R. Natoli, Electron population analysis by full-potential X-ray absorption simulations, Phys. Rev. Lett. 82 (1999) 2398–2401. doi:10.1103/PhysRevLett.82.2398.

[31] D.J. Kim, D.S. Kim, S. Cho, S.W. Kim, S.H. Lee, J.C. Kim, Measurement of thermal conductivity of TiO2 thin films using 3ω method, Int. J. Thermophys. 25 (2004) 281–289. doi:10.1023/B:IJOT.0000022340.65615.22.

[32] M.-H. Hong, S.-Y. Jung, T.-J. Ha, W.-S. Seo, Y.S. Lim, S. Shin, H.H. Cho, H.-H. Park, Thermoelectric properties of mesoporous TiO2 thin films through annealing temperature and ratio of surfactant, Surf. Coatings Technol. 231 (2013) 370–373. doi:10.1016/j.surfcoat.2012.07.035.

[33] L. Xu, M.P. Garrett, B. Hu, Doping effects on internally coupled seebeck coefficient, electrical, and thermal conductivities in aluminum-doped TiO 2, J. Phys. Chem. C. 116 (2012) 13020–13025. doi:10.1021/jp302652c.

[34] D. Kurita, S. Ohta, K. Sugiura, H. Ohta, K. Koumoto, Carrier generation and transport properties of heavily Nb-doped anatase TiO[sub 2] epitaxial films at

high temperatures, J. Appl. Phys. 100 (2006) 096105. doi:10.1063/1.2362990.

[35] S. Ohta, T. Nomura, H. Ohta, M. Hirano, H. Hosono, K. Koumoto, Large thermoelectric performance of heavily Nb-doped SrTiO 3 epitaxial film at high temperature, Appl. Phys. Lett. 87 (2005) 1–4. doi:10.1063/1.2035889.

[36] L. Sheppard, T. Bak, J. Nowotny, C.C. Sorrell, S. Kumar, A.R. Gerson, M.C. Barnes, C. Ball, Effect of niobium on the structure of titanium dioxide thin films, Thin Solid Films. 510 (2006) 119–124. doi:10.1016/j.tsf.2005.12.272.

[37] A. Janotti, C. Van Walle, Fundamentals of zinc oxide as a semiconductor, Reports Prog. Phys. 72 (2009) 126501. doi:10.1088/0034-4885/72/12/126501.

[38] A. Fujishima, T.N. Rao, D.A. Tryk, Titanium dioxide photocatalysis, J. Photochem. Photobiol. C Photochem. Rev. 1 (2000) 1–21. doi:10.1016/S1389-5567(00)00002-2.

[39] E. Burstein, Anomalous optical absorption limit in InSb [4], Phys. Rev. 93 (1954) 632–633. doi:10.1103/PhysRev.93.632.

Institute of Solid State Physics, University of Latvia as the Center of Excellence has received funding from the European Union's Horizon 2020 Framework Programme H2020-WIDESPREAD-01-2016-2017-TeamingPhase2 under grant agreement No. 739508, project CAMART²